Supplementary Materials for

A Bipolar Spindle Of Antiparallel ParM Filaments Drives Bacterial Plasmid Segregation

P. Gayathri, T. Fujii, J. Møller-Jensen, F. van den Ent, K. Namba, J. Löwe*

*To whom correspondence should be addressed. E-mail: jyl@mrc-lmb.cam.ac.uk

Published 25 October 2012 on *Science* Express
DOI: 10.1126/science.1229091

This PDF file includes:

Other Supplementary Material for this manuscript includes the following:
available at www.sciencemag.org/cgi/content/full/science.1229091/DC1

Materials and Methods

Expression and purification

ParM (UniProt PARM_ECOLX), its mutants and ParR (UniProt STBB_ECOLX) were expressed from the plasmids *pJSC1* and *pJSC21*, respectively (*10*), in *E. coli* BL21-AI cells and purified as described previously (*1*, *7*). Brief details of the purification are described below.

ParM and ParR were finally gel filtrated into a common buffer (Buffer MR: 50 mM Tris-HCl, 100 mM KCl, and 1 mM $MgCl_2$, pH 7.0), and this buffer was used in all further experiments. Concentrated aliquots of pure protein were frozen and stored at -80 °C.

Wild type ParM: Wild type ParM was purified by ammonium sulfate precipitation (at a final concentration of 10 % (sat.) ammonium sulfate) of the lysate, followed by addition of ATP to the resuspended pellet. The polymerized ParM was pelleted by centrifugation at 50,000 *g*, and the resulting pellet containing pure protein was resuspended in buffer and gel filtrated on a Sephacryl S-200 column (GE Healthcare). Wild type ParM used for TIRF experiments was purified from the lysate using a HiTrap Q HP column (GE Healthcare), instead of ammonium sulfate precipitation. The fractions containing ParM were pooled and further purified using the ATP polymerization step. ParM used for ITC and TIRF experiments were treated with EDTA and then gel filtrated on a Superdex 200 10/300 GL column (GE Healthcare), to ensure complete removal of nucleotide.

ParM(L163R) mutant: The N-terminally 6xHis-tagged protein was expressed from plasmid *pJMJ101* (*pTTQ19* derivative). The protein was purified using a 5 ml HisTrap column (GE Healthcare), and eluted using a gradient of imidazole. The fractions containing ParM were pooled and further purified using a HiTrap Q HP column (GE Healthcare), and then dialyzed into 10 mM Tris HCl, 10 mM KCl, 1mM $MgCl_2$, pH 7.5.

ParM(L163A) mutant: Instead of the polymerization step using ATP in the protocol for the wild type ParM, after ammonium sulfate precipitation the sample was purified using a HiTrap Q HP (GE Healthcare) column with sufficient dilution to allow binding. The pure fractions were pooled after elution, concentrated and gel filtrated.

ParM(S19R,G21R) and ParM(S19E,G21E) mutants: the same purification protocol as described for the ParM wild type protein was followed.

ParR: 1,10-phenanthroline was included as a protease inhibitor in the lysis buffer to prevent proteolytic cleavage of ParR. As described previously (*7*), the purification steps included a HiTrap Heparin column and HiTrap SP HP cation exchange column, and gel filtration (Sephacryl S300, all GE Healthcare). The size of purified full-length ParR was confirmed by ESMS mass spectrometry since proteolysis occurs easily.

Crystallization, data collection and structure refinement

Crystallization conditions were identified from a high-throughput screen (*25*) using 100 nl of protein and 100 nl of the crystallization solution, in sitting drop vapor diffusion MRC plates.

ParM-AMPPNP complex: ParM(L163R) was stored in 10 mM Tris-HCl, 10 mM KCl, 1 mM $MgCl_2$, pH 7.5, and 5 mM AMPPNP (adenosine 5′-(β,γ-imido) triphosphate, tetralithium salt) and 10 mM $MgCl_2$ were added prior to crystallization. Crystals were obtained in 20 % PEG 6000, 100 mM Bicine pH 8.6, 1 M LiCl, at 10 mg/ml

concentration of the protein, and cryoprotected with additional 24 % PEG 400. Diffraction data was collected at beamline ID29 (ESRF, Grenoble, France).

ParM-AMPPNP-ParR$_{pept}$ complex: The protein sample for crystallization consisted of 10 mg/ml (final concentration) ParM(L163A) mixed with 5 mM of ParR$_{pept}$ (H_2N-EQKSDEETKKNAMKLIN-COOH; residues 101 to 117 of ParR; Advanced Biomedical Ltd, UK), 10 mM AMPPNP and 10 mM $MgCl_2$. Crystals were obtained in 0.1 M citric acid pH 5.0, and 2.4 M ammonium sulfate. The crystals were flash-frozen in liquid nitrogen after cryoprotection using 40 % sodium malonate solution, pH 7.0. Diffraction data were collected at beamline ID14-2 (ESRF, Grenoble, France).

The data collection and refinement statistics are summarized in Table S1. The data sets were processed using MOSFLM (*26*) and molecular replacement solutions were obtained using PHASER (*27*). Model building and refinement were performed using COOT (*28*) and PHENIX (*29*), respectively. The quality of the structure was validated using the MolProbity server (*30*).

Register of the peptide was confirmed by anomalous dispersion from data collected at beamline I02 (Diamond Light Source, Harwell, UK) from a crystal containing selenomethionine (SeMet)-labeled peptide (synthesized with Met-113 replaced by SeMet; Advanced Biomedicals Ltd., UK; Fig. S2A).

The coordinates have the Protein Data Bank (PDB) accession codes 4A61 and 4A62 for the ParM-AMPPNP and ParM-AMPPNP-ParR$_{pept}$ structures, respectively.

Electron microscopy

ParM filaments for electron microscopy were prepared by incubating 30 μM protein in 200 μl polymerization buffer (30 mM Tris-HCl, 25 mM KCl, 2 mM $MgCl_2$, 1 mM DTT, pH 7.5) with 5 mM AMPPNP for 5 min at room temperature. The filaments were pelleted by centrifugation for 60 min at 100,000 *g* to remove monomers, and resuspended in 40 μl buffer. A 2.1 μl sample solution was applied onto a Quantifoil holey carbon molybdenum grid (R0.6/1.0, Quantifoil Micro Tools GmbH, Jena, Germany) and was plunge-frozen into liquid ethane using a fully automated vitrification device (Vitrobot, FEI). The specimen was observed at temperatures of 50 – 60 K using a JEOL JEM3200FSC electron microscope, which is equipped with a liquid-helium cooled specimen stage, an Ω-type energy filter and a field-emission electron gun operated at 200 kV. Zero energy-loss images, with a slit setting to remove electrons of an energy-loss larger than 10 eV, were recorded on a 4k × 4k 15 μm/pixel slow-scan CCD camera, TemCam-F415MP (TVIPS, Germany) at a magnification of 91,463, a defocus range of 0.7 – 2.0 μm and an electron dose of ~20 electrons/Å^2. The magnification was calibrated by measuring the layer line spacing of 23.0 Å in the Fourier transform of images of tobacco mosaic virus mixed in the sample solution. The image pixel size at this magnification was 1.64 Å/pixel. In total of 200 CCD images were collected.

Defocus and astigmatism in the images were determined using CTFFIND3 (*31*). Images of the ParM filament from the 200 CCD frames were boxed into 20917 segments of 512 × 512 pixels with a step shift of 100 pixels along the helical axis using EMAN's boxer program (*32*). The in-plane orientation of each ParM filament was retained in the segment and recorded in a list to avoid interpolation when rotating the image. Images were then phase-corrected by multiplying a phase and amplitude contrast transfer function (CTF) with the astigmatism obtained by CTFFIND3

(*32*). We used a ratio of 7 % for the amplitude CTF to the phase CTF (*33*). This procedure for the CTF correction results in the multiplication of the square of the CTF (CTF^2) to the original structure factor and suppresses the noise around the nodes of the CTF, allowing more accurate image alignment. The amplitude modification by CTF^2 was corrected in the last stage of image analysis as described later. The images were then high-pass filtered (285 Å) to remove any low spatial frequency density undulation, normalized and cropped to 320 × 320 pixels. Image processing was mainly carried out with the SPIDER package (*34*) on a PC cluster computer with 40 CPUs (RC server Calm2000, Real Computing, Tokyo, Japan).

A series of reference projection images were generated for each reference volume by rotating the volume azimuthally about the filament axis between 0º and 360º and projecting the volume every 1º to produce all views. The raw images of the boxed ParM segments were translationally and rotationally aligned and cross-correlated with the set of reference projections to produce the following information: an in-plane rotation angle, an x-shift, a y-shift, an azimuthal angle and a cross-correlation coefficient for each segment. Particles with a small cross-correlation coefficient were discarded. The polarity of the particles was tracked with respect to their respective filament. Even with our high contrast imaging technique, the orientation of each individual particle was somewhat ambiguous due to the relatively low contrast and high noise level of the segment image. Therefore, the orientation was defined as that of the majority of the particles for each filament during each alignment cycle, and all the segments identified to have the opposite orientation were discarded. A 3D reconstruction was then generated by back-projection. The symmetry of this new volume was determined by a least-squares fitting algorithm, and this symmetry was imposed upon the reconstruction (*35*). The new symmetry-enforced volume was used as a reference for the next round of alignment. This process was repeated iteratively until the symmetry values converged to a stable solution.

In the analysis, the polarities of the segment images were determined reliably. On average, the in-plane angles for 95% of the segments from a ParM filament showed the same polarity. The initial parameters were an axial rise of 24.7 Å and an azimuthal rotation angle of 163º along the 1-start helix, and they were converged to 23.62 Å and 164.98º, respectively. The resulting reconstruction was then modified by multiplying the transform of the reconstruction by $1/[\sum CTF^2 + 1/SNR]$ to compensate for the amplitude distortion by the contrast transfer function. The map was sharpened with a B-factor of -200 $Å^2$. Table S2 gives the statistics of the EM reconstruction.

The atomic coordinates of the filament were obtained by fitting the ParM:$ParR_{pept}$ conformation of the monomer into the filament map, and then generating the rest of the subunits by applying the helical parameters. The EM reconstruction has been deposited in the EMDB (EMD-1980), and the fitted coordinates in the PDB (4A6J).

Isothermal Calorimetry (ITC)

ITC experiments were performed using a MicroCal iTC_{200} machine with a ParM concentration of 20 μM and $ParR_{pept}$ at 1 mM in the cell and syringe, respectively. Nucleotide, when included, was added at a concentration of 10 mM in both the syringe and the cell. An initial injection of 0.5 μl and twenty injections of 2 μl each of the peptide were added into the cell at intervals of 120 s with constant stirring at 1000 rpm. The data was analyzed using Origin software as provided by the manufacturer. The estimated K_d value is the mean value from three independent measurements.

Fluorescent labeling

A single AlexaFluor label was incorporated on ParM monomers through an 11-residue peptide tag (DSLEFIASKLA) at the N-terminus (ParM-Sfp) by site-specific labeling using Sfp synthase (*36*). CoA-conjugated AlexaFluor derivatives were synthesized according to (*37*). Fluorescent labeling was done by incubation at room temperature for 3 hours in a 100 μl reaction mix containing 90 μM ParM-Sfp, 1 mM CoA-conjugated AlexaFluor dye, 50 mM HEPES pH 7.5, 10 mM $MgCl_2$, and 2 μM of Sfp synthase. ParM monomers capable of polymerization were selected from the reaction mix by a few rounds of pelleting at 100,000 *g* after addition of ATP. The pellet obtained was resuspended in buffer containing EDTA and then gel filtrated to remove the excess nucleotide and free dye. The labeling efficiency was estimated using the ratio of absorbance of the protein and the dye using a NanoDrop ND1000 spectrophotometer. The final concentrations of protein and dye were estimated to be 25 μM and 0.9 μM for ParM-Alexa568, and 16 μM and 4 μM for ParM-Alexa488. 20 μl aliquots were flash-frozen and stored at -80 °C.

For labeling the ParR*C* complex, YOYO-1 (Molecular Probes), a DNA intercalating dye, was used to label the plasmid DNA. 200 nM of YOYO-1 was added to a mixture of 10 μM of ParR and 10 nM of *parC* (plasmid *pMD330*) (*38*) in a 50 μl reaction mix. This was dialyzed extensively overnight in 500 ml of buffer, and resulted in an increase in volume to about 150 μl. The labeled sample was freshly prepared each time and used for TIRF microscopy experiments within 24 hours. The formation of the R*C* complex was confirmed by gel shift assays (data not shown).

For experiments with QDot labeled ParR*C*, a 385-bp PCR product containing the *parC* sequence was amplified using the primers SR14 and biotinylated-SR15 (*7*) with *pMD330* as template, for producing biotin-tagged DNA. This was labeled using QDot 545-Streptavidin conjugate (Invitrogen), and used for reconstituting the ParR*C* complex at a 1:40 molar ratio of *parC* to ParR. The concentrations of Q-Dot labelled ParR*C* mentioned in the text refer to the final molar concentration of *parC*.

TIRF microscopy

Imaging: Imaging was performed on an Olympus IX71 TIRF microscope, using a 60x 1.49 NA objective, equipped with an Evolve EMCCD camera (Photometrics). Micro-Manager 1.4 was used for image acquisition (*39*). Dual-channel images were collected using a custom-made image splitter in the path of the beam before entering the camera. Physical pixel size corresponds to 83 nm in object space after applying the magnification introduced by the settings of the microscope and the splitter. The images were split into the two channels using the Cairn Image Splitter plugin in Fiji (http://imageja.sourceforge.net) based on a reference image obtained from FocalCheck microspheres (Invitrogen). The channels were merged to obtain the composite images. Data were acquired continuously as movies of 500 images at 100 ms exposure time per image. The images were filtered by applying a Gaussian blur with a sigma of 1. All image-processing steps involving the stacks of images were performed in Fiji. The rates of elongation and disassembly reported were calculated as slope of the kymographs of filaments, and are tabulated (Table S3).

Experimental set-up: A 1:1000 ratio of labeled to unlabeled ParM was maintained in all reactions, in order to obtain speckled filaments for better contrast. The speckled appearance also serves as fiducial points. 1 % methylcellulose (crowding agent to maintain the filaments in the TIRF field) was included in Buffer MR, and 50 nM protocatechuate-3,4-dioxygenase, 2.5 mM protocatechuic acid and 1 mM of Trolox as antibleach reagents (*40*) added to the reaction mix. The final concentration of methylcellulose in the reaction mix was 0.9 % after addition of all other components of the mixture. The reaction mix was transferred to a chamber of a Lab-Tek 8-chambered borosilicate coverslip system for imaging, immediately after initiating polymerization by the addition of the nucleotide. The chambers were pre-treated by incubation with 10 mg/ml of β-casein for at least 30 minutes. The experiments for observing unwinding of the spindle were performed in a reaction mix containing 0.45 % methylcellulose.

Dual-label experiments for observing bidirectional growth: Polymerization was initiated in a reaction mix containing a single color of Alexa-labeled ParM, and growth of filaments was observed. ParM monomers labeled with the second color were added to the chamber while imaging, and the focus was readjusted on a field containing dual-labeled filaments. The fluorescence intensity of parts of the filaments with the second label was higher compared to the initial seed due to the inadequate mixing of the labeled ParM added later. The experiment was performed with and without ParR*C*. The portion of the filament after the initial seed will contain both the labels, since they are both present, with the second label at a higher intensity. Unlabeled ParM concentrations used were in the range of 0.4 to 1 μM. ParR*C* complex was prepared by mixing 5 μM of ParR and 5 nM of *pMD330*, and 1 to 2 μl were added to the 200 μl reaction mixture before initiating polymerization with 2 mM (final concentration) AMPPNP. The rate of growth was estimated for the two ends of the same filament from the slopes of the kymographs.

Dual-channel imaging of ParRC at the tip of ParM filaments: Unlabeled ParM concentrations in the range of 0.4 to 1 μM were used along with 2 to 4 μl of the dialyzed YOYO-1-labeled ParR*C* complex, in a 200 μl reaction. 2 mM AMPPNP or ATP was used as the nucleotide. The rates of spindle elongation and disassembly were estimated from the slopes of the lines manually fitted onto the kymographs. *parC* labeled with streptavidin-conjugated QDot 545 (Invitrogen) was used for estimating the number of ParM filaments with 0, 1 or 2 ends bound to ParR*C*. The images were obtained at very low ParM concentrations of 0.35– 0.4 μM to minimize spontaneous nucleation of ParM filaments unaided by ParR*C*. The bipolar spindles reported for ParM wild-type and the interface mutants were obtained using Q-Dot labelled ParR*C*. The rate of spindle elongation was estimated from YOYO-1 labeled ParR*C*. The rates of elongation and disassembly are tabulated in Table S3.

Contributions:

PG: performed and devised all experiments not mentioned below and wrote the manuscript

TF: performed EM helical reconstruction of ParM filaments

JMJ: determined ParM-AMPPNP crystal structure with FvdE

FvdE: determined ParM-AMPPNP crystal structure with JMJ

KN: supervised TF and devised experiments

JL: devised experiments, supervised and wrote the manuscript

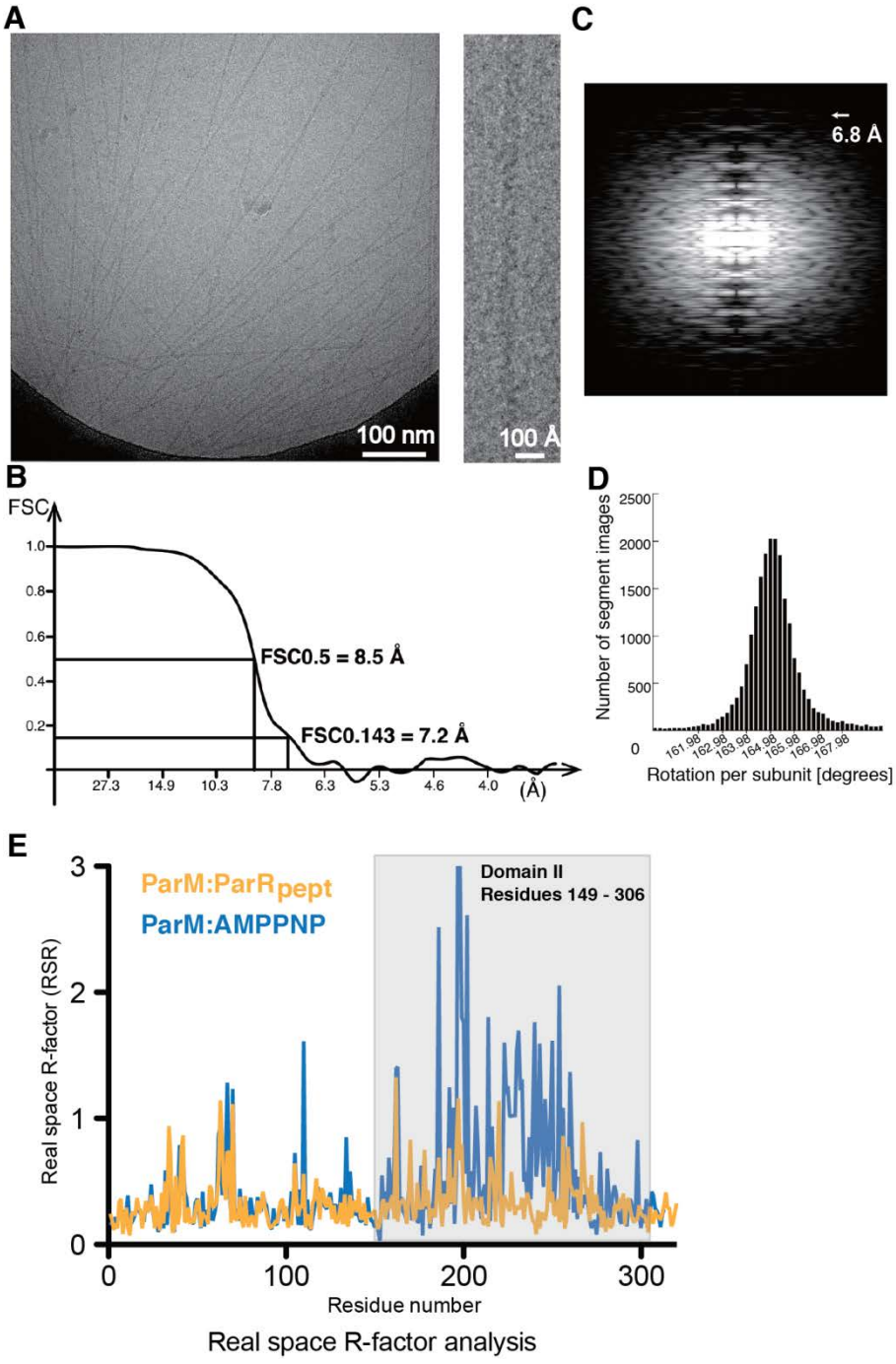

Fig. S1. Electron cryomicroscopy of ParM filaments.

A) Left: a representative micrograph of ParM filaments. Right: a zoomed view of a single filament. B) Fourier shell correlation function (FSC) to estimate the resolution of the three-dimensional reconstruction of the ParM filament. FSC at 0.5 demonstrates a resolution of 8.5 Å C) Power spectrum of the 3D reconstruction showing layer lines up to 6.8 Å. D) Histogram showing distribution of rotation angles per subunit after image processing. E) Real space R-factor analysis to quantitate the fit of ParM:$ParR_{pept}$ and ParM:AMPPNP conformations in the EM reconstruction of ParM filament. The monomer conformations were fitted into the EM reconstruction with the residues 1-148 and 307-320 of domain I as reference, using Chimera (*24*). The residue-wise real space R-factor (RSR) of the fit was

calculated using MAPMAN (Uppsala Software Factory; www.xray.bmc.uu.se/usf), and plotted. The difference between the R-factors in domain II for the two conformations is highlighted. The plot for ParM:ParR$_{pept}$ and the overall real space R-factors (0.33 and 0.47 for ParM:ParR$_{pept}$ and ParM:AMPPNP, respectively) confirms the excellent fit of the conformation in the density.

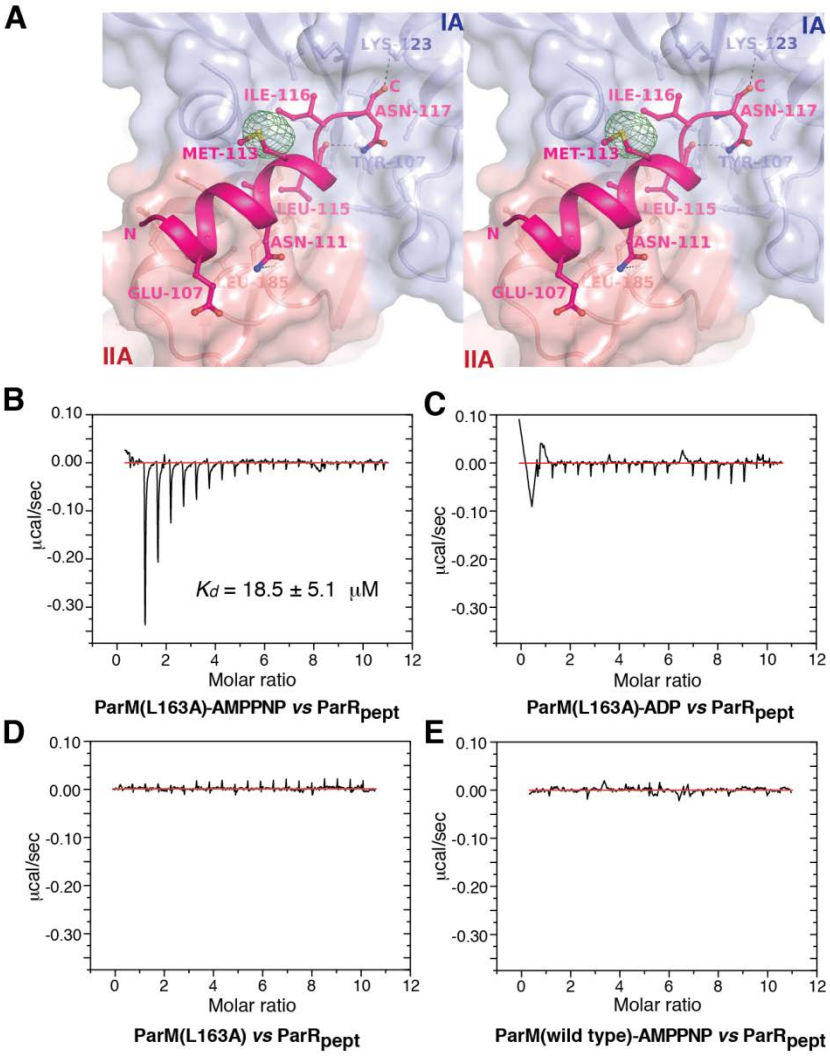

Fig. S2. Interactions between ParM and ParR.

A) $ParR_{pept}$ binds within a predominantly hydrophobic pocket formed by residues from subdomains IA and IIA, at the polymerization interface. The C-terminal COOH moiety of $ParR_{pept}$ interacts with Lys-123 of ParM (*10*). Superimposed is the anomalous map at 2.5 σ for selenium in the crystal structure of ParM with $ParR_{pept}$ in which Met-113 is replaced by seleno-methionine. The position of the peak confirms the register of the peptide fitted into the electron density map. The figure is shown in wall-eyed stereo and the same color scheme as in Figure 2 is followed. B-E) ITC data for ParM(L163A) mutant titrated with $ParR_{pept}$ in the presence of AMPPNP (B), in the presence of ADP (C), and without nucleotide (D), ParM wild type in the presence of AMPPNP (polymerized ParM) (E). The peptide binds with a K_d of 18.5 ± 5.1 µM to a non-polymerizing mutant of ParM(L163A) in the presence of AMPPNP, while no binding is detected to polymerized ParM or in the absence of nucleotide or in the presence of ADP. The flat binding curve when polymerized ParM is titrated against the peptide rules out the possibility of peptide-binding along the sides of the filament. Peptide-binding to the filament ends cannot be detected by ITC in the experimental conditions used, since the concentration of filament ends in the polymerized sample is too low to produce detectable levels of binding energy.

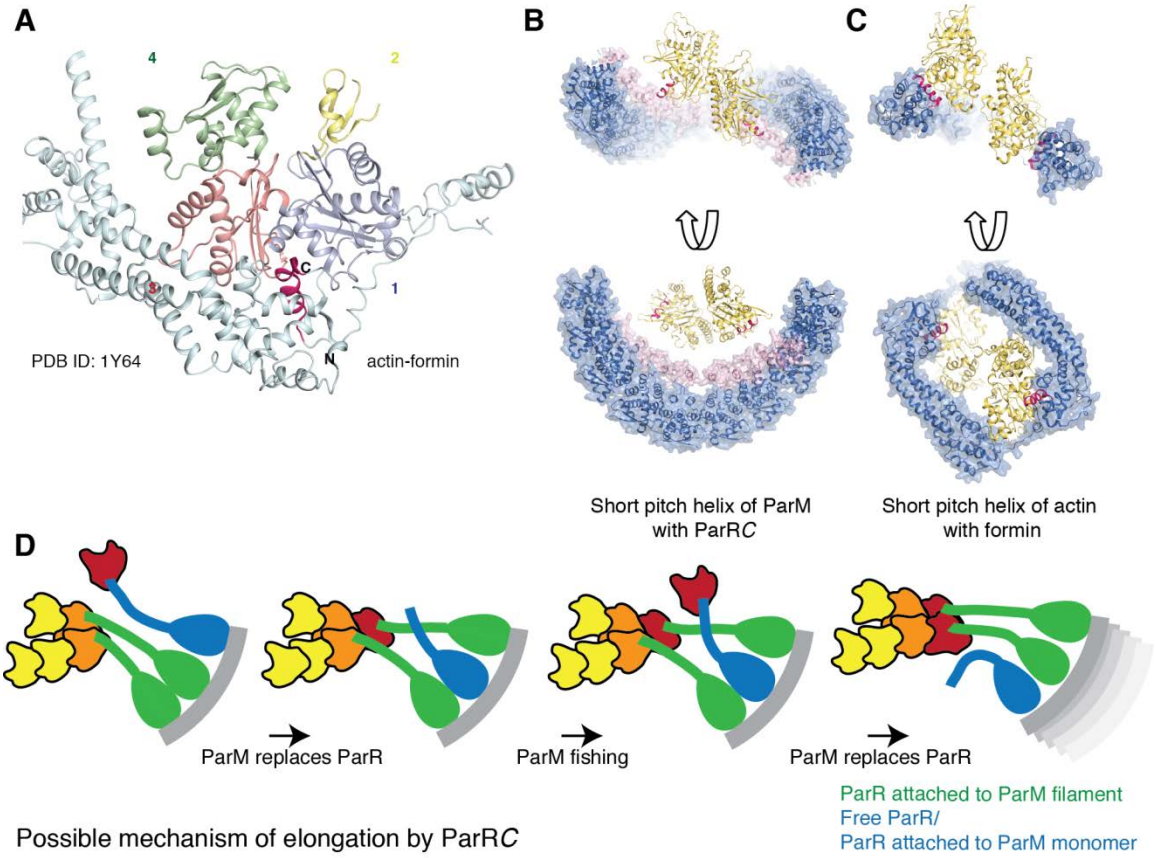

Fig. S3. Mechanism of ParR-assisted ParM filament elongation.

A) A helix in FH2 domain of formin (highlighted in dark pink) binds between subdomains 1 and 3 of actin, corresponding to the interaction between $ParR_{pept}$ and ParM (see also Figure 2A). B-C) The scaffold formed by formin and ParR*C* matches the geometry of the short-pitch helix of actin and ParM. Two adjacent monomers that form the short pitch helix are shown for actin and ParM (yellow) along with the formin and ParR*C* scaffolds (blue; cartoon and surface representation), respectively. With allowance for the flexible stretch of residues between the ParR N-terminal domain and the C-terminal helix, the geometry of the ParR*C* ring approximates the dimension of the short pitch helix of ParM filament. Residues 1-94 of the ParR N-terminal domain are shown in surface and cartoon representation in blue with residues 86-94 highlighted in pink, while the C-terminal helix (residues 101-117) bound to ParM is shown in dark pink. Side and bottom views are shown. D) A putative mechanism of ParM filament elongation by ParR*C*. Two ParRs (in green) of the ParR*C* ring are bound to the filament, while a third ParR (in blue) fishes for ATP-bound ParM monomers (in red) from the vicinity. The monomer recruited into the ParR*C* ring displaces one of the filament-bound ParRs and is incorporated into the filament.

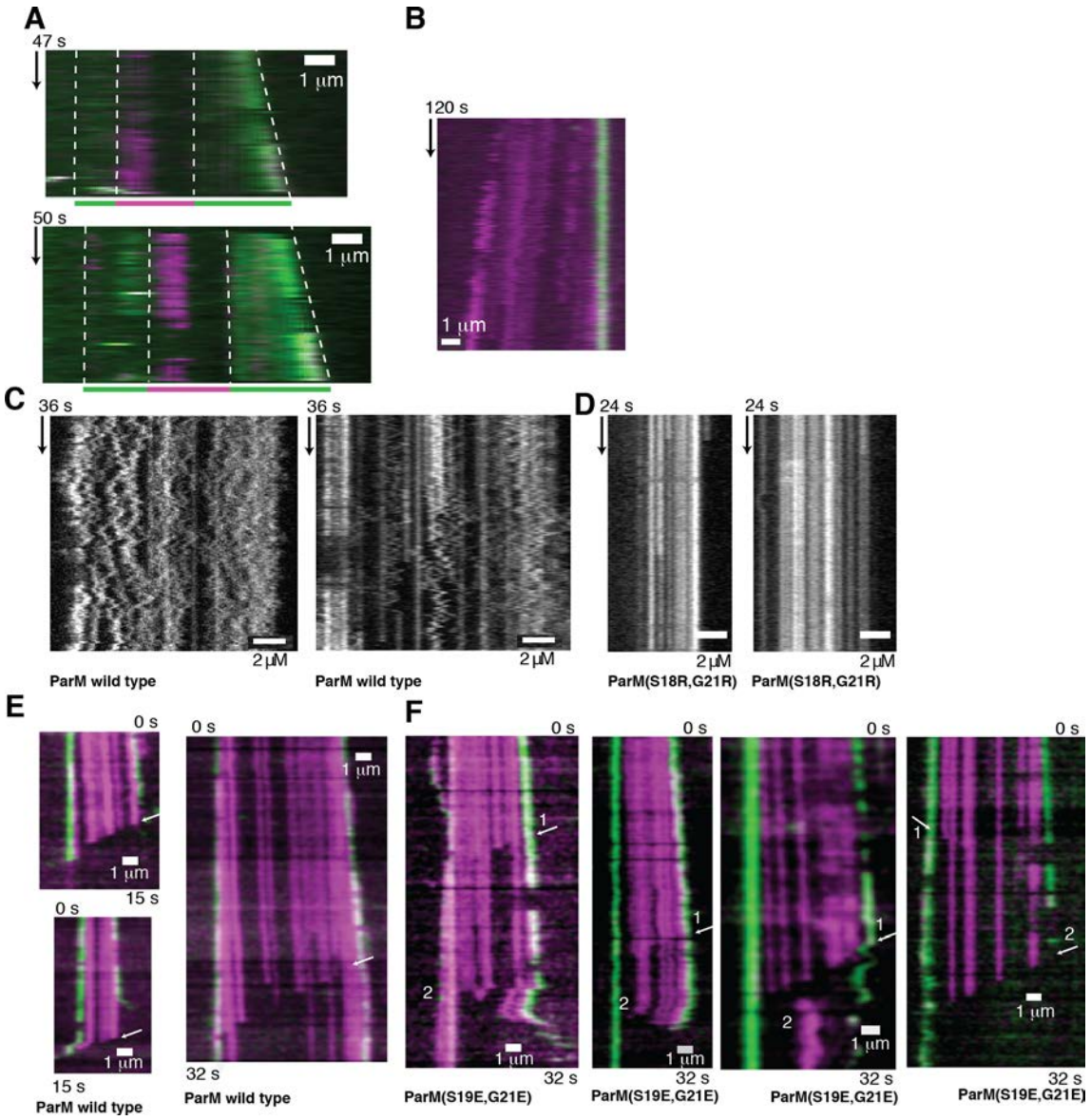

Fig. S4. Bipolar spindles are formed by antiparallel ParM filaments.

A) More examples of kymographs corresponding to filaments in a dual label experiment with ParR*C* (see also Figure 3B of main text). Boundaries of the filament and the initial seed are highlighted. B) Another example of a kymograph from ParM filaments labeled with Alexa-568 and ParR*C* (green) labeled using YOYO-1 is shown (see also Figure 3C). C) More examples of observation of zigzag movement of filaments in kymographs of bundles of wild-type ParM filaments (see also Figure 4A). D) More examples of static filaments in kymographs of bundles of ParM(S19R,G21R) filaments (see also Figure 4D). E-F) More examples for kymographs of disassembling spindles of ParM wild-type (E) and ParM(S19E,G21E) (F). The arrows highlight the slopes of the disassembly events. The two steps of disassembly, evident in the kymographs of the partially unpaired ParM(S19E,G21E) mutant spindles, have been marked. The two-step disassembly is not evident in the disassembly of most of the wild type spindles, since the two component filaments disassemble simultaneously.

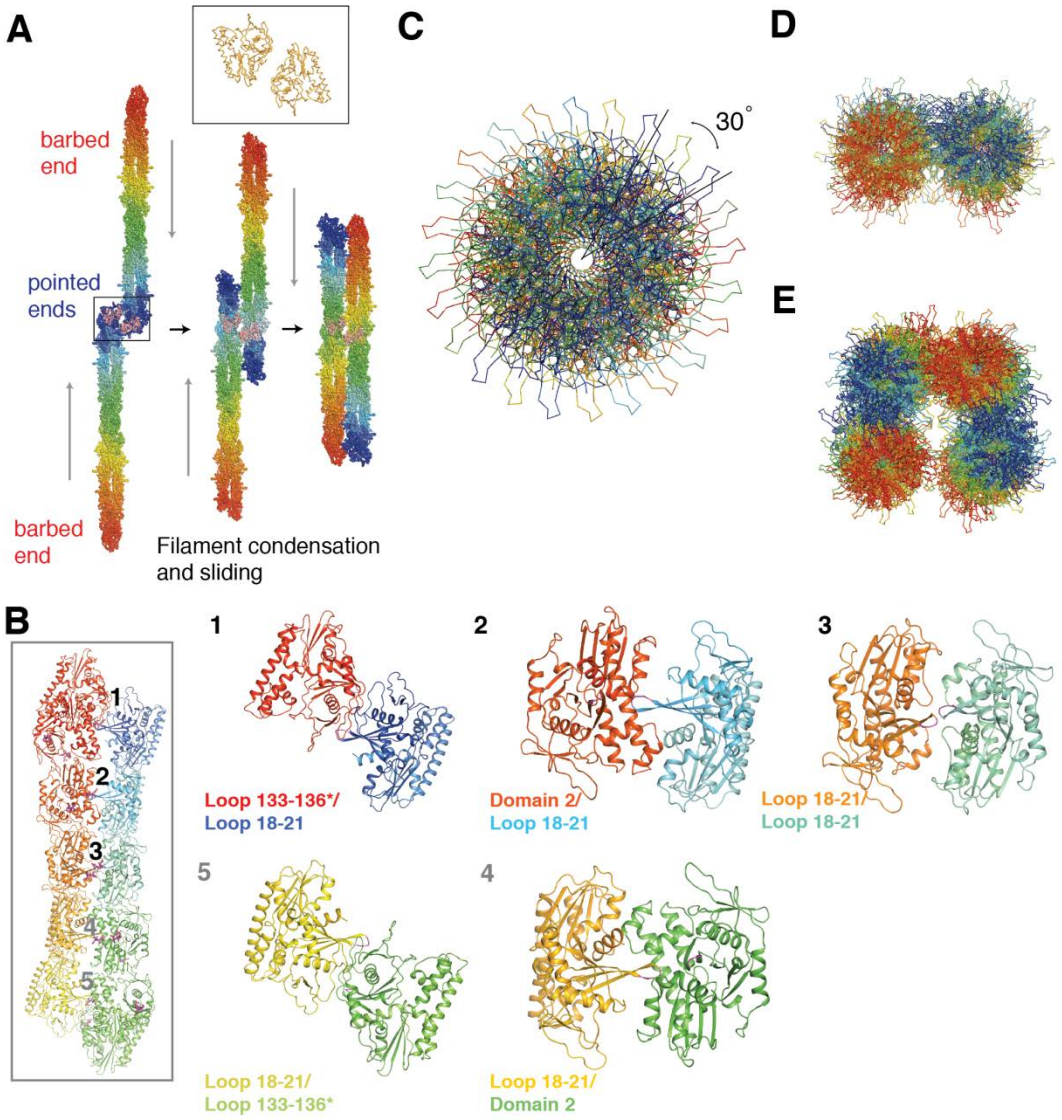

Fig. S5. A molecular model for antiparallel ParM filaments.
A) A model for filament condensation. Subunits of ParM filaments are superposed sequentially onto the ParM monomers in antiparallel orientation (inset) in the crystal packing of the ParM:ParR$_{pept}$ complex, resulting in 'sliding' and an antiparallel packing of two filaments. The grey arrows indicate the direction of sliding. B) Interfaces between the two antiparallel ParM filaments. A segment of the final step of the antiparallel model in (A) is shown in the inset and the interfaces between two monomers are numbered. The details of the numbered interfaces are also shown. It should be noted that (1) & (5) and (2) & (4) are similar interfaces. All the interfaces involve loop 18-21 which is the position of the mutations designed in this study. C) The 12-fold symmetry of the ParM helix is compatible with a tight hexagonal or square packing of ParM filaments. D-E) Axial views of antiparallel ParM bundles consisting of 2 (D) and 4 (E) filaments respectively.

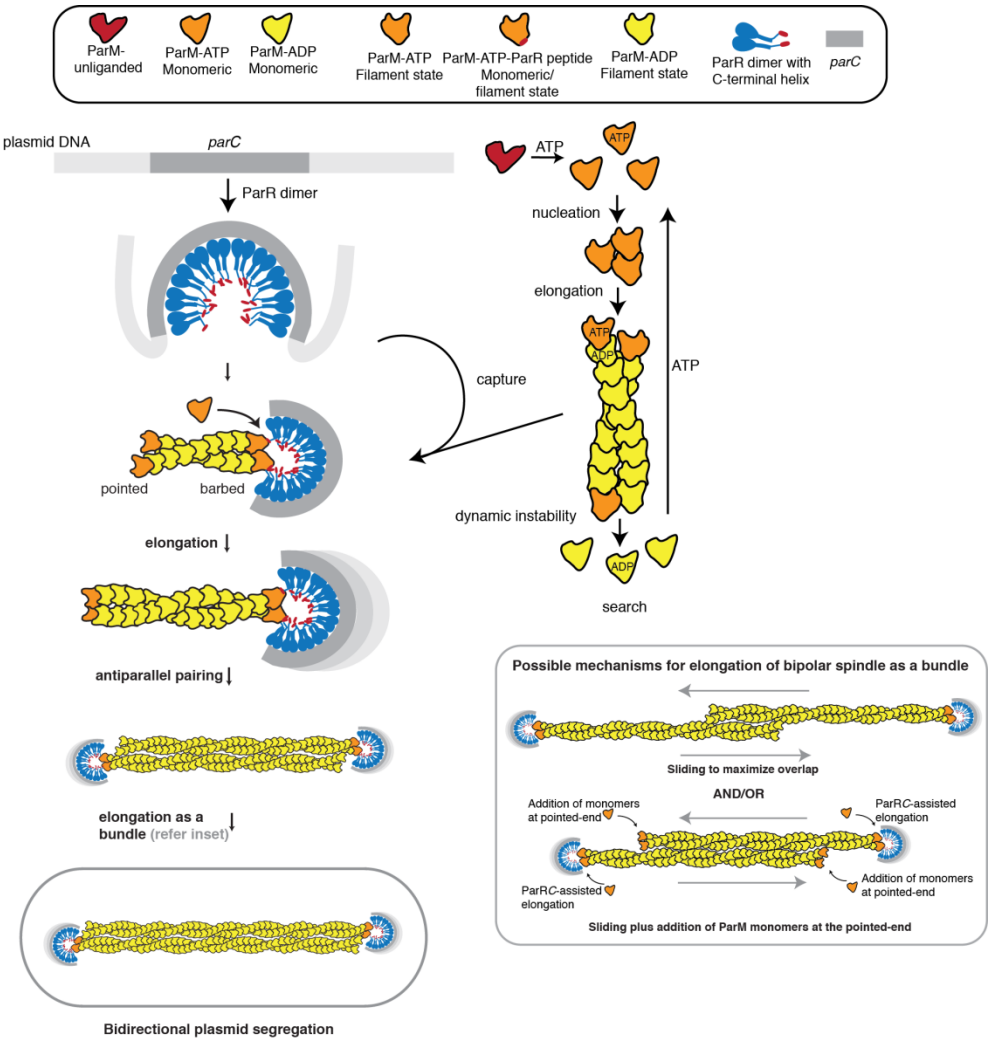

Fig. S6. A comprehensive model of plasmid segregation by ParMRC.
A schematic diagram summarizing the proposed events in plasmid segregation by ParMRC. ParM goes through cycles of spontaneous polymerization and depolymerization through nucleation, elongation and dynamic instability (top right). For the filaments to be rescued from catastrophic disassembly, they have to be captured by the ParRC complex. We demonstrate here that the ParRC complex binds only at the barbed-end of the ParM filament. The other end of the filament becomes protected when two filaments come together to form an antiparallel bundle. The result is a bipolar spindle with plasmids bound at each end through the ParRC adaptor complexes. Addition of new subunits at each end will lead to elongation. The elongating spindle grows as a bundle at all times, possibly by concomitant sliding to maximize overlap, and/or by addition of ParM monomers at the pointed-end also (inset). Addition of subunits at the pointed-end is facilitated by additional binding energy that is available to the incoming subunits, provided by the neighboring filament in the bundle. In a similar way, dynamic instability is stopped by the stabilization of the terminal subunits at the pointed-end through the provision of extra binding energy by the neighboring filament. The bundles may contain more than two filaments, in order to segregate larger numbers of plasmids.

Table S1. Data collection and refinement statistics for ParM-AMPPNP and ParM-AMPPNP-ParR$_{pept}$ structures.

(ParM: UniProt PARM_ECOLX, ParR: UniProt STBB_ECOLX)

Data collection	ParM-AMPPNP	ParM-AMPPNP-ParR$_{pept}$	ParM-AMPPNP-ParR$_{pept\text{-}SeMet}$
Sample	H_6-2-ParML163R	ParML163A:ParR(101-117)	same, SeMet
Wavelength [Å]	0.9762	0.933	0.9795
Space Group	$P4_322$	H32	H32
Unit cell, a, c [Å]	63.5, 164.1	146.8, 171.3	146.2, 166.6
Resolution [Å]	50.0 - 2.0	50.0 - 2.2	50.0 - 3.0
Mean (I/σI)*	12.1 (2.3)	20.0 (4.4)	16.8 (5.6)
R_{merge} [%]*,†	9.2 (51.0)	8.3 (51.9)	10.5 (42.3)
Multiplicity*	6.3 (3.8)	10.3 (9.6)	10.6 (10.9)
Completeness [%]*	98.4 (90.9)	100 (100)	100 (100)
Anomalous multiplicity*			5.4 (5.5)
Anomalous completeness [%]*			100 (100)
Refinement			
ParM	1 chain residues 0-210, 218 -240, 246-320	2 chains residues 1-320	
ParR$_{pept}$		2 chains residues 105-117	
Ligands	1 AMPPNP, 1 Mg^{2+}, 138 wat.	2 AMPPNP, 2 Mg^{2+} 162 waters	
Resolution range [Å]	43.3 – 2.0	32.6 – 2.2	
R_{work} [%]	20.9	20.0	
R_{free} [%]‡	25.3	26.8	
Mean B-factor [Å^2]	35.21	31.56	
Bond length, RMSD [Å]	0.005	0.006	
Bond angle, RMSD [degrees]	0.936	1.016	
Residues in Ramachandran plot §			
Favoured [%]	96.7	96.5	
Disallowed [%]	0.0	0.0	
PDB ID	**4A61**	**4A62**	

* Values for the highest resolution shell are given in parenthesis.

† $R_{merge} = \underset{h}{\Sigma}\underset{l}{\Sigma} | I_{hl} - \langle I_h \rangle_{h} | \underset{l}{/} \Sigma\Sigma \langle I_h \rangle$

‡ 5 % of the reflections were included in the test set.

§ Values obtained from PROCHECK (*41*).

Table S2. Statistics of ParM EM reconstruction.

Number of micrographs	207
Magnification	x91,436
Pixel size	1.64 Å/pixel
Total number of segmented images in initial selection	20,917
Total number of segmented images	15,634
Number of asymmetric units	108,546
Resolution (FSC = 0.143)	7.2 Å
Resolution (FSC = 0.5)	8.5 Å
Helical symmetry	
Translation	23.621 Å
Rotation	164.98°
Fitted PDB ID	**4A6J**
EMDB ID	**EMD-1980**

Table S3. Summary of rates of elongation and disassembly of ParM filaments / spindles.

	Nucleotide	ParR*C*	Rate, nm/s	Rate, Subunits/s [*]	*n* [†]
ParM-AMPPNP[‡]	AMPPNP	Plasmid *pMD330* labelled with YOYO-1	22.3 ± 9.8	9.4 ± 4.1	32
ParM-AMPPNP ParR*C*-bound end[‡]			6.0 ± 4.6	2.5 ± 1.9	32
ParM – no ParR*C*[§]	ATP	-	NA	NA	-
ParM - ParR*C*	ATP	Plasmid *pMD330* labelled with YOYO-1	14.7 ± 3.2	6.2 ± 1.3	14
ParM - ParR*C*[¶]	ATP	Biotinylated 385-bp PCR amplified fragment labelled with streptavidin-linked Q-Dot	53.5 ± 11.3	22.6 ± 4.8	40
ParM disassembly	ATP	Biotinylated 385-bp PCR amplified fragment labelled with streptavidin-linked Q-Dot	234.8 ± 44.2	100.3 ± 18.7	61

[*] Rate in subunits/s = Rate in nm/s / Rise per subunit (2.36 nm).
[†] Number of observations.
[‡] The rates with and without ParR*C* have been estimated from two ends of the same filament.
[§] Filaments are too short and do not remain in evanescent field to determine the rate of growth accurately.
[¶] The difference between rates of spindle elongation with YOYO-1 labeled plasmid and PCR fragment of *parC* could be due to the differences in the size of the DNA, and also due to differences in efficiency of ParR*C* complex formed. We found that YOYO-1, an intercalating dye, displaces ParR.

Movie S1. The ParM:ParR$_{pept}$ conformation fits best into the EM reconstruction of the ParM filament.
Movie showing a morph between the fit of the ParM:ParR$_{pept}$ and ParM-AMPPNP conformations into a monomer segment of the filament map. Residues 1-160 and 305-320 of domain I were used for rigid-body fitting using Chimera (*24*). The morph shows a clear movement of domain II in the ParM:ParR$_{pept}$ state resulting in a better fit compared to the ParM-AMPPNP state.

Movie S2. The Growth of ParM filaments without ParRC is bidirectional and symmetric.
Alexa488-labeled (green) ParM monomers were added to filaments growing in the presence of Alexa568-labeled (magenta) ParM monomers with AMPPNP as the nucleotide. The movie was obtained using a reaction mix containing 0.5 μM ParM and 2 mM AMPPNP. Figure 3A in the main text shows a kymograph of one of the filaments in the movie. The middle segments (initial seed) of the filaments become photobleached as the movie progresses, while the intensity of the flanking growing ends are higher. The filament that enters into the field towards the end of the movie clearly shows the symmetric growth on either end of the initial magenta seed. The lengths (in micrometers) of the flanking regions are highlighted at the end of the movie. The movie was made using averages of ten original frames.

Movie S3. ParR*C* accelerates growth unidirectionally, resulting in bidirectional but asymmetric growth.
ParR*C* increases the rate of growth of ParM filaments in one of the directions, resulting in asymmetry. Alexa488-labeled (green) ParM monomers were added to filaments growing in the presence of Alexa568-labeled (magenta) ParM monomers and unlabeled ParR*C* with AMPPNP as the nucleotide. The movie was obtained using a reaction mix containing 0.5 μM ParM, 2 mM AMPPNP, and 1 μl of ParR*C* mixture. The movie was made using averages of five original frames.

Movie S4. Insertional polymerization by ParR*C*.
ParR*C* binds to one end of a single filament and monomers are recruited at the ParR*C*-binding end, leading to insertional polymerization. ParM filaments were labeled with Alexa-568, while ParR*C* was labeled using the intercalating dye YOYO-1. The movie was obtained using a 200 μl reaction mix containing 0.4 μM ParM and 2 mM AMPPNP, and 2 μl of back-dialyzed ParR*C*, labeled with YOYO-1. The movie was made using averages of five original frames.

Movies S5 and S6. Filament sliding and bundling of ParM filaments grown in the presence of ATP.
ParM filaments form bundles by interfilament sliding. Magenta arrows highlight the filament bundles that slide together to form a bigger bundle. The movies were obtained using a reaction mix containing 2.5 μM ParM and 2 mM ATP. These bundles also exhibit dynamic instability when individual filaments slide out of the bundle and disassemble. The movies were made using averages of five original frames.

Movies S7 and S8. Filament sliding and bundling of ParM filaments grown in the presence of AMPPNP.
The movies were obtained using a reaction mix containing 2.5 μM and 4 μM ParM, respectively, with 2 mM AMPPNP. Six observations of sliding events are highlighted in Movie S7. Movie S7 was made using averages of three original frames. Figure 4A shows a montage from Movie S8.

Movies S9 and S10. To and fro sliding in bundles of ParM filaments.
Continuous motion of labeled monomers within ParM filament bundles, due to growth followed by sliding. The movies were obtained with samples containing 2.5 μM and 4 μM ParM respectively, and 2 mM AMPPNP. The kymographs in Figure 4B and Figure S4C correspond to filaments from Movie S9.

Movie S11. To and fro sliding of ParM filaments in two colors.
Two separate samples of ParM at 2.5 μM concentration, containing Alexa488 and Alexa568 labeled monomers respectively, were polymerized using 2 mM AMPPNP, and then added to opposite corners of the experimental chamber. The sample was observed at different regions of the chamber, to observe smaller filaments labeled with

Alexa488 sliding over thicker bundles labeled with Alexa568. Two channels (488 nm and 561 nm), and their merge are shown.

Movie S12. Filament sliding does not occur in bundles of the ParM(S19R,G21R) mutant.
ParM(S19R,G21R) was polymerized at the same conditions as the wild type (Movie S7), at 2.5 μM concentration with 2 mM AMPPNP. The filaments within the bundles do not slide. Longer bundles are observed since the bundles do not slide against each other and condense.

Movies S13 and S14. Bipolar spindles formed by ParM in the presence of ParR*C* and ATP.
Elongating spindles formed by samples containing 0.5 μM ParM and 2.5 nM Q-Dot labeled ParR*C*, and polymerized with 2 mM ATP are shown. The movies were made using averages of three original frames.

Movies S15 and S16. Spindle disassembly triggered by detachment of ParR*C*.
The detachment of ParR*C* leads to disassembly of the bipolar spindle. The movies were obtained using samples containing low concentrations of wild type ParM (0.35 μM), 2.5 nM Q-Dot labeled ParR*C*, polymerized with 2 mM ATP.

Movie S17. A bipolar spindle is formed by two antiparallel ParM filaments.
Spindles obtained using ParM(S19E,G21E) mutant are unstable, and disassemble due to unpairing of the filaments in the spindle. The movie shows an example in which the component filaments separate, clearly demonstrating that the spindle is composed of two antiparallel ParM filaments, with ParR*C* bound at one end of each. The splitting of the filaments leads to unstable (pointed) ends, leading to dynamic instability of ParM filaments, and disassembly of the spindle. The movie was obtained at 0.5 μM ParM(S19E,G21E), 2.5 nM Q-Dot labeled ParR*C*, and polymerized with 2 mM ATP, and the sample buffer contained 0.45 % methylcellulose. It may be required to watch this movie frame-by-frame in order to be able to follow all events.

Movie S18. Two-step disassembly of ParM filaments in a bipolar spindle.
Disassembly is triggered in one of the filaments in a spindle obtained using ParM(S19E,G21E) mutant due to detachment of ParR*C* (top). The disassembly in this filament is followed by the disassembly of the other filament due to loss of the stabilizing interaction with the paired filament. The distinct disassembly events of the two filaments are clearly observed because of the partial unpairing of the filaments in the mutant. In a wild-type spindle, it is very difficult to distinguish the disassembly of the two component filaments since they support each other for stability and disassemble simultaneously. The movie was obtained at 0.5 μM ParM(S19E,G21E), 2.5 nM Q-Dot labeled ParR*C*, and polymerized with 2 mM ATP, and the sample buffer contained 0.45 % methylcellulose. Spindles of wild type ParM do not unwind under the same conditions. It may be required to watch this movie frame-by-frame in order to be able to follow all events.

Movie S19. Spindle disassembly triggered by unpairing of filaments.
Another example of a spindle formed by ParM(S19E, G21E) mutant that disassembles due to unpairing of the filaments. The filaments slide apart, leading to disassembly of the spindle. The filament ends are marked using white and yellow arrowheads to highlight the sliding event. The movie was obtained at 0.5 μM ParM(S19E,G21E), 2.5 nM Q-Dot labeled ParR*C*, and polymerized with 2 mM ATP and the sample buffer contained 0.45 % methylcellulose. It may be required to watch this movie frame-by-frame in order to be able to follow all events.

References and Notes

1. F. van den Ent, J. Møller-Jensen, L. A. Amos, K. Gerdes, J. Löwe, F-actin-like filaments formed by plasmid segregation protein ParM. *EMBO J.* **21**, 6935 (2002). doi:10.1093/emboj/cdf672 Medline

2. D. Popp *et al.*, Molecular structure of the ParM polymer and the mechanism leading to its nucleotide-driven dynamic instability. *EMBO J.* **27**, 570 (2008). doi:10.1038/sj.emboj.7601978 Medline

3. K. Gerdes, M. Howard, F. Szardenings, Pushing and pulling in prokaryotic DNA segregation. *Cell* **141**, 927 (2010). doi:10.1016/j.cell.2010.05.033 Medline

4. J. Salje, P. Gayathri, J. Löwe, The ParMRC system: molecular mechanisms of plasmid segregation by actin-like filaments. *Nat. Rev. Microbiol.* **8**, 683 (2010). doi:10.1038/nrmicro2425 Medline

5. E. C. Garner, C. S. Campbell, R. D. Mullins, Dynamic instability in a DNA-segregating prokaryotic actin homolog. *Science* **306**, 1021 (2004). doi:10.1126/science.1101313 Medline

6. E. C. Garner, C. S. Campbell, D. B. Weibel, R. D. Mullins, Reconstitution of DNA segregation driven by assembly of a prokaryotic actin homolog. *Science* **315**, 1270 (2007). doi:10.1126/science.1138527 Medline

7. J. Møller-Jensen, S. Ringgaard, C. P. Mercogliano, K. Gerdes, J. Löwe, Structural analysis of the ParR/parC plasmid partition complex. *EMBO J.* **26**, 4413 (2007). doi:10.1038/sj.emboj.7601864 Medline

8. M. A. Schumacher *et al.*, Segrosome structure revealed by a complex of ParR with centromere DNA. *Nature* **450**, 1268 (2007). doi:10.1038/nature06392 Medline

9. C. L. Choi, S. A. Claridge, E. C. Garner, A. P. Alivisatos, R. D. Mullins, Protein-nanocrystal conjugates support a single filament polymerization model in R1 plasmid segregation. *J. Biol. Chem.* **283**, 28081 (2008). doi:10.1074/jbc.M803833200 Medline

10. J. Salje, J. Löwe, Bacterial actin: architecture of the ParMRC plasmid DNA partitioning complex. *EMBO J.* **27**, 2230 (2008). doi:10.1038/emboj.2008.152 Medline

11. See Supporting Online Materials in *Science Online*.

12. T. Fujii, A. H. Iwane, T. Yanagida, K. Namba, Direct visualization of secondary structures of F-actin by electron cryomicroscopy. *Nature* **467**, 724 (2010). doi:10.1038/nature09372 Medline

13. T. Oda, M. Iwasa, T. Aihara, Y. Maéda, A. Narita, The nature of the globular- to fibrous-actin transition. *Nature* **457**, 441 (2009). doi:10.1038/nature07685 Medline

14. T. Otomo *et al.*, Structural basis of actin filament nucleation and processive capping by a formin homology 2 domain. *Nature* **433**, 488 (2005). doi:10.1038/nature03251 Medline

15. M. Hertzog *et al.*, The beta-thymosin/WH2 domain; structural basis for the switch from inhibition to promotion of actin assembly. *Cell* **117**, 611 (2004). doi:10.1016/S0092-8674(04)00403-9 Medline

16. R. Dominguez, Actin-binding proteins—a unifying hypothesis. *Trends Biochem. Sci.* **29**, 572 (2004). doi:10.1016/j.tibs.2004.09.004 Medline

17. B. L. Goode, M. J. Eck, Mechanism and function of formins in the control of actin assembly. *Annu. Rev. Biochem.* **76**, 593 (2007). doi:10.1146/annurev.biochem.75.103004.142647 Medline

18. J. Møller-Jensen, R. B. Jensen, J. Löwe, K. Gerdes, Prokaryotic DNA segregation by an actin-like filament. *EMBO J.* **21**, 3119 (2002). doi:10.1093/emboj/cdf320 Medline

19. J. Møller-Jensen *et al*., Bacterial mitosis: ParM of plasmid R1 moves plasmid DNA by an actin-like insertional polymerization mechanism. *Mol. Cell* **12**, 1477 (2003). Medline

20. J. Salje, B. Zuber, J. Löwe, Electron cryomicroscopy of *E. coli* reveals filament bundles involved in plasmid DNA segregation. *Science* **323**, 509 (2009). doi:10.1126/science.1164346 Medline

21. C. S. Campbell, R. D. Mullins, In vivo visualization of type II plasmid segregation: bacterial actin filaments pushing plasmids. *J. Cell Biol.* **179**, 1059 (2007). doi:10.1083/jcb.200708206 Medline

22. D. Popp *et al*., Concerning the dynamic instability of actin homolog ParM. *Biochem. Biophys. Res. Commun.* **353**, 109 (2007). doi:10.1016/j.bbrc.2006.11.130 Medline

23. S. X. Sun, S. Walcott, C. W. Wolgemuth, Cytoskeletal cross-linking and bundling in motor-independent contraction. *Curr. Biol.* **20**, R649 (2010). doi:10.1016/j.cub.2010.07.004 Medline

24. E. F. Pettersen *et al*., UCSF Chimera—a visualization system for exploratory research and analysis. *J. Comput. Chem.* **25**, 1605 (2004). doi:10.1002/jcc.20084 Medline

25. D. Stock, O. Perisic, J. Löwe, Robotic nanolitre protein crystallisation at the MRC Laboratory of Molecular Biology. *Prog. Biophys. Mol. Biol.* **88**, 311 (2005). doi:10.1016/j.pbiomolbio.2004.07.009 Medline

26. A. G. Leslie, The integration of macromolecular diffraction data. *Acta Crystallogr. D Biol. Crystallogr.* **62**, 48 (2006). doi:10.1107/S0907444905039107 Medline

27. A. J. McCoy *et al*., Phaser crystallographic software. *J. Appl. Cryst.* **40**, 658 (2007). doi:10.1107/S0021889807021206 Medline

28. P. Emsley, K. Cowtan, Coot: model-building tools for molecular graphics. *Acta Crystallogr. D Biol. Crystallogr.* **60**, 2126 (2004). doi:10.1107/S0907444904019158 Medline

29. P. D. Adams *et al*., PHENIX: a comprehensive Python-based system for macromolecular structure solution. *Acta Crystallogr. D Biol. Crystallogr.* **66**, 213 (2010). doi:10.1107/S0907444909052925 Medline

30. V. B. Chen *et al*., MolProbity: all-atom structure validation for macromolecular crystallography. *Acta Crystallogr. D Biol. Crystallogr.* **66**, 12 (2010). doi:10.1107/S0907444909042073 Medline

31. J. A. Mindell, N. Grigorieff, Accurate determination of local defocus and specimen tilt in electron microscopy. *J. Struct. Biol.* **142**, 334 (2003). doi:10.1016/S1047-8477(03)00069-8 Medline

32. S. J. Ludtke, P. R. Baldwin, W. Chiu, EMAN: semiautomated software for high-resolution single-particle reconstructions. *J. Struct. Biol.* **128**, 82 (1999). doi:10.1006/jsbi.1999.4174 Medline

33. K. Yonekura, M. B. Braunfeld, S. Maki-Yonekura, D. A. Agard, Electron energy filtering significantly improves amplitude contrast of frozen-hydrated protein at 300kV. *J. Struct. Biol.* **156**, 524 (2006). doi:10.1016/j.jsb.2006.07.016 Medline

34. J. Frank *et al.*, SPIDER and WEB: processing and visualization of images in 3D electron microscopy and related fields. *J. Struct. Biol.* **116**, 190 (1996). doi:10.1006/jsbi.1996.0030 Medline

35. E. H. Egelman, A robust algorithm for the reconstruction of helical filaments using single-particle methods. *Ultramicroscopy* **85**, 225 (2000). doi:10.1016/S0304-3991(00)00062-0 Medline

36. J. Yin *et al.*, Genetically encoded short peptide tag for versatile protein labeling by Sfp phosphopantetheinyl transferase. *Proc. Natl. Acad. Sci. U.S.A.* **102**, 15815 (2005). doi:10.1073/pnas.0507705102 Medline

37. J. Yin, A. J. Lin, D. E. Golan, C. T. Walsh, Site-specific protein labeling by Sfp phosphopantetheinyl transferase. *Nat. Protoc.* **1**, 280 (2006). doi:10.1038/nprot.2006.43 Medline

38. M. Dam, K. Gerdes, Partitioning of plasmid R1. Ten direct repeats flanking the parA promoter constitute a centromere-like partition site *parC*, that expresses incompatibility. *J. Mol. Biol.* **236**, 1289 (1994). doi:10.1016/0022-2836(94)90058-2 Medline

39. A. Edelstein, N. Amodaj, K. Hoover, R. Vale, N. Stuurman, Computer control of microscopes using microManager. *Curr Protoc Mol Biol* **Chapter 14**, Unit 14.20 (2010).

40. C. E. Aitken, R. A. Marshall, J. D. Puglisi, An oxygen scavenging system for improvement of dye stability in single-molecule fluorescence experiments. *Biophys. J.* **94**, 1826 (2008). doi:10.1529/biophysj.107.117689 Medline

41. R. A. Laskowski, D. S. Moss, J. M. Thornton, Main-chain bond lengths and bond angles in protein structures. *J. Mol. Biol.* **231**, 1049 (1993). doi:10.1006/jmbi.1993.1351 Medline